Catalysis Today 175 (2011) 26–33

Contents lists available at ScienceDirect

Catalysis Today

journal homepage: www.elsevier.com/locate/cattod

# The reaction of NO + $C_3H_6$ + $O_2$ over the mesoporous SBA-15 supported transition metal catalysts

Runduo Zhang, Dongjun Shi, Yanli Zhao, Biaohua Chen*, Jun Xue, Xin Liang, Zhigang Lei

*State Key Laboratory of Chemical Resource Engineering, Beijing University of Chemical Technology, Beijing 100029, PR China*

ARTICLE INFO

*Article history:*
Received 20 September 2010
Received in revised form 25 January 2011
Accepted 6 April 2011
Available online 8 May 2011

*Keywords:*
Mesoporous
SBA-15
NO reduction
Propene
Copper

ABSTRACT

A series of mono-functional M/SBA-15 (*M* = Cu, Fe, Cr, and Al) and bifunctional M′/SBA-15 (M′ = Cu–Al, Fe–Al, and Cr–Al) catalysts was prepared via an incipient wetness impregnation, and further characterized by $N_2$ adsorption, XRD, TEM, $H_2$-TPR, $Al^{27}$-NMR, and XPS as well as activity test for $C_3H_6$ + NO + $O_2$ reaction. Ordered mesoporous structure of SBA-15 was well maintained even after impregnating the various metallic components. The *de*$NO_x$ activities of investigated catalysts follow a trend of Cu–Al/SBA-15 > Cu/SBA-15, Fe/SBA-15 > Cr–Al/SBA-15 > Cr/SBA-15 ≫ Fe–Al/SBA-15, Al/SBA-15 > SBA-15. Synergistic effect between copper and alumina was achieved showing a satisfactory NO conversion of approximately 80% over Cu–Al/SBA-15 at temperature as low as 350 °C under an atmosphere of 3000 ppm NO, 3000 ppm $C_3H_6$, 1% $O_2$ and GHSV of 60,000 $h^{-1}$. The SCR performance was found to be strongly correlated to the redox properties of tested catalysts, essentially chemical nature of supported metals, and surface density of active metallic species.



## 1. Introduction

The use of hydrocarbons as reducing agents (commonly with propene as a model delegate) for the catalytic reduction of hazardous nitrogen oxides, which are emitting from the automobile engines and can cause acid rain and photochemical smog, currently attracts much attention [1,2]. Great effort has been made in order to improve the three-way performances of catalytic converters aiming at satisfying the requirement of increasingly strict regulations for environmental protection. Noble metal-supported oxides have already been commercialized as three-way catalysts; however, the scarcity and relatively high price of noble metals (e.g. Pt, Rh, Pd, etc.) limit their practical application. Attempts were subsequently made to use molecular sieves mainly focusing on ZSM-5, Y, and Beta-type zeolites doped with cheap transition metals for the NO reduction [3–5]. Unfortunately, the pore blockage of these microporous zeolites due to the deposition of carbonaceous and sulfurous species in the exhaust effluent represents a fatal problem.

Mesostructured zeolites constitute a new state of association of molecular sieves having regularly spatial arrangement of pores with monodimensional size distribution tunable in the range of 2–50 nm. These nanoscaled materials promise spectacular improvement of catalytic activity in many reactions owing to their high specific surface areas and precise control of their surface chemistry [6,7]. Their relatively larger pore sizes as compared to those of microporous zeolites facilitate the transportation of reactants and might lead to a better resistance to $SO_2$ and steam poisoning as well as deactivation caused by pore blockage. Simultaneously, their unique feature of superhigh surface area is beneficial for good dispersion of active metallic components. Among the mesoporous zeolites, newly achieved SBA-15 exhibits excellent thermal stability and was thought as promising candidate acting as a support of some industrial catalysts [6]. SBA-15 is by far one of the largest pore-size mesoporous material with highly ordered and hexagonally arranged mesochannels, adjustable pore sizes from 3 to 30 nm, and high hydrothermal and thermal stability [6]. Nevertheless, reports related to the utilization of mesostructured SBA-15 for the catalytic reduction of NO with $C_3H_6$ are so far scarce in the literature.

In the present study, a series of SBA-15-based catalysts including parent SBA-15, mono-functional M (M = Cu, Cr, Fe, and Al)/SBA-15, and bifunctional M′ (M′ = Cu–Al, Cr–Al, and Fe–Al)/SBA-15 was prepared and characterized by $N_2$ adsorption, X-ray diffraction (XRD), transmission electron microscopy (TEM), temperature programmed reduction by hydrogen ($H_2$-TPR), nuclear magnetic resonance (NMR), X-ray photoelectron spectroscopy (XPS) as well as the activity tests for catalytic reduction of NO with $C_3H_6$ in the presence of $O_2$. Emphasis will be placed on clarifying the relationship between the physicochemical properties of prepared catalysts and their depollution performances.

* Corresponding author. Tel.: +86 10 64412054; fax: +86 10 64436787.
*E-mail addresses:* zhangrd@mail.buct.edu.cn (R. Zhang), chenbh@mail.buct.edu.cn (B. Chen).

0920-5861/$ – see front matter © 2011 Elsevier B.V. All rights reserved.
doi:10.1016/j.cattod.2011.04.014

## 2. Experimental

### 2.1. Catalyst preparation

The mesoporous SBA-15 was synthesized by a template method as described in detail in the previous paper [6]. For a typical synthesis, 4.0 g of P123 [$EO_{20}PO_{70}EO_{20}$, poly(ethylene glycol)-block-poly(propylene glycol)-block-poly(ethylene glycol), average molecular weight = 5800, Aldrich] was dissolved into 90 ml deionized water at ambient temperature under violent stirring. Subsequently, 60 ml of 4 M HCl (CR, Chuangqi) was introduced with continuous stirring. 9.8 ml of tetraethyl orthosilicate (TEOS, CR, Damao) was added dropwise into the former solution at 40 °C. After being stirred continuously for 24 h, the mixture was transferred to a Teflon-lined stainless steel autoclave and placed in an oven at 100 °C for 24 h. The precipitate was in turn filtered, washed with deionized water, and dried at room temperature. The obtained powders were finally heated up to 550 °C at a ramp rate of 1 °C/min and calcined at this temperature in air for 24 h.

Metal-containing samples of (Cu, Cr, Fe, Al, Cu–Al, Cr–Al, and Fe–Al)/SBA-15 with ~1 mol% loading for each component (a molecular weight of $SiO_2$ was used for the corresponding calculation of SBA-15) were prepared by means of an incipient wetness impregnation method. The bare SBA-15 was impregnated into an ethanol solution containing a desired amount of metal nitrate. Thereafter, this solution was transferred into a vacuum evaporator to eliminate the solvent. The residue was dried at 110 °C for 2 h and further calcined at 550 °C for 5 h.

### 2.2. Catalyst characterization

X-ray diffraction (XRD) patterns were acquired on a Rigaku D/max 2500VB2 diffractometer operating at 40 kV and 200 mA with Cu *K*α irradiation and nickel filter (λ = 0.15406 nm). The XRD patterns were recorded in the 2$\theta$ range of 0.5–10° for small-angle profiles. The *d* space ($d_{100}$) was estimated from the position of the low-angle peak in the range of 9.8–10.4 nm. The unit cell parameter ($a_0$) was calculated using the equation of $a = 2d_{100}/\sqrt{3}$.

Specific surface areas, pore-size distributions, pore total volumes and sorption isotherms of the solids were measured via $N_2$ adsorption/desorption at −196 °C using an automated gas sorption system (Sorptomatic 1990, Thermo Electron) with all samples outgassed at 300 °C for 4 h under vacuum before the measurement. Specific surface areas and pore-size distributions were calculated according to the Brunauer–Emmett–Teller (BET) and Barrett–Joyner–Halenda (BJH) methods, respectively. Micropore volume ($V_{micro}$) was obtained by using *t*-plot method.

The morphology of powder was studied by high resolution transmission electron microscopy (HRTEM) with a magnification of 500,000× using a JEOL J-3010 instrument operated at 200 kV. In order to understand the nature of the catalyst surface, X-ray photoelectron spectroscopy (XPS) was conducted on a Thermofisher ESCALAB 250 system with Al *K*α radiation under ultrahigh vacuum (UHV), calibrated internally by carbon deposit C (1 s) binding energy (BE) at 284.6 eV. $^{27}$Al magic angle spinning nuclear magnetic resonance (MAS NMR) spectra were collected by a Varian Infinity Plus 300 MHz spectrometer to identify the Al status.

Temperature programmed reduction by hydrogen ($H_2$-TPR) was conducted inside a fixed-bed reactor with samples (about 200 mg) in situ pretreated by 20 ml/min $O_2$/He flow at 500 °C for 0.5 h. After cooling down to room temperature under the same atmosphere, the tested sample was exposed to 20 ml/min of 5% $H_2$/Ar and heated at a rate of 10 °C/min up to 900 °C. $H_2$ consumption was on-line monitored by thermal conductivity detector (TCD) using a flow of 20 $cm^3$/min of 5% $H_2$/Ar as reference gas. The gas responses obtained by TCD were calibrated using the corresponding standard gases containing known concentrations of the components.

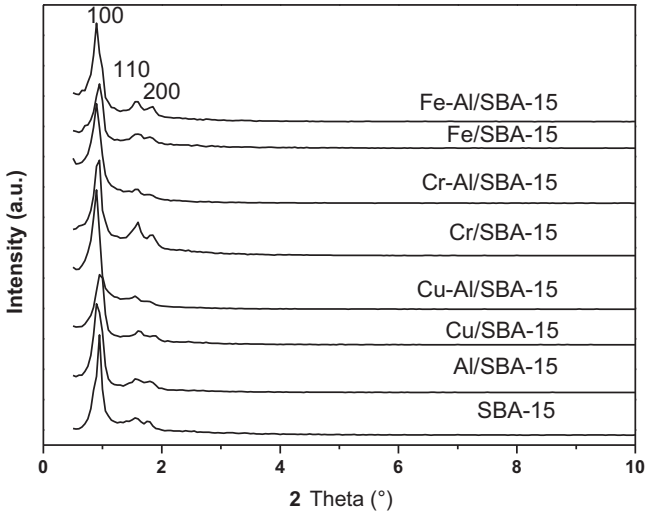


**Fig. 1.** Small-angle XRD patterns of SBA-15, (Al, Cu, Cr, Fe)/SBA-15, and (Cu, Cr, Fe)-Al/SBA-15.

### 2.3. Activity test

Activity measurement was performed in a quartz fixed-bed reactor (3 cm i.d.) loading with ~0.2 g catalyst under an atmosphere of 3000 ppm NO, 3000 ppm $C_3H_6$, 1% $O_2$, balanced by He with a total flow rate of 100 ml/min (corresponding to a space velocity of approximately 60,000 $h^{-1}$). The reactor was regulated continuously using a temperature controller with a thermocouple inserted into the catalyst bed achieving temperatures from 200 to 600 °C by steps of 50 °C. The effluent gases (NO, $N_2O$, $C_3H_6$, CO and $CO_2$) were monitored using an infrared gas analyzer (Nicolet Nexus 670) equipped with a 2.4 meter long-path gas cell and TQ analysis software, while $N_2$ and $O_2$ were monitored using a gas chromatograph (GC, 6890; Lu'nan) equipped with TCD and separated by a column of 5A molecular sieve. Nitrogen oxides (NO and $NO_2$) were simultaneously analyzed using a chemiluminescence NO/$NO_2$/$NO_x$ analyzer. Nitrogen balance for detected N-containing products ($N_2$, NO, $N_2O$, and $NO_2$) was achieved with an error within 5%.

## 3. Results and discussion

### 3.1. Structural characterization

Fig. 1 shows the small-angle XRD patterns of as-synthesized SBA-15-based samples without and with metal (Fe, Cu, Cr, and/or Al) doping. Three diffraction peaks at 2$\theta$ = 0.94, 1.6, and 1.8° were clearly discernable from the corresponding profile for the parent SBA-15 in Fig. 1 which could be respectively indexed as (1 0 0), (1 1 0) and (2 0 0) *h k l* reflections of *P6mm* symmetry having a *d*-spacing of the (1 0 0) plane of 9.4 nm and cell parameter of $a_0$ = 10.8 nm, as listed in Table 1. The formation of typical SBA-15 silica with well-ordered and hexagonally structured mesoporous channels was thus verified, according to the earlier study [6]. With the introduction of various metals (Fe, Cu, Cr and Al), this mesoporous structure of SBA-15 could be basically retained showing those characteristic peaks for (1 0 0), (1 1 0) and (2 0 0) reflections in the case of all investigated samples. However, a drop in intensity of the main diffraction peaks in the small-angle region occurred along with Fe–Al, Cr–Al, Cu–Al, and Cr addition, reflecting the appearance of some deterioration of the ordered pore structures. This decline

**Table 1**
Characteristics of the mesoporous SBA-15-based catalysts.

| Sample | BET area ($m^2$/g) | Pore volume ($cm^3$/g) | | | Pore diameter (nm) | $d_{100}$ (nm) | Cell parameter $a_0$ (nm) | Wall thickness (nm) |
|---|---|---|---|---|---|---|---|---|
| | | Micropore | Mesopore | Total | | | | |
| SBA-15 | 645 | 0.10 | 0.71 | 0.81 | 8.0 | 9.4 | 10.8 | 2.8 |
| Al/SBA-15 | 403 | 0.18 | 0.55 | 0.73 | 7.6 | 9.8 | 11.3 | 3.7 |
| Cu/SBA-15 | 593 | 0.13 | 0.71 | 0.84 | 7.4 | 9.3 | 10.8 | 3.4 |
| Cu–Al/SBA-15 | 441 | 0.07 | 0.53 | 0.60 | 6.2 | 9.8 | 11.3 | 5.1 |
| Cr/SBA-15 | 568 | 0.13 | 0.48 | 0.61 | 6.8 | 9.3 | 10.8 | 4.0 |
| Cr–Al/SBA-15 | 575 | 0.08 | 0.61 | 0.69 | 6.9 | 9.7 | 11.2 | 4.3 |
| Fe/SBA-15 | 614 | 0.11 | 0.74 | 0.85 | 7.5 | 9.3 | 10.8 | 3.3 |
| Fe–Al/SBA-15 | 513 | 0.19 | 0.61 | 0.80 | 5.2 | 9.7 | 11.2 | 6.0 |

in the intensity of XRD peaks at around 0.94° became serious for the Cu/SBA-15, Fe/SBA-15, and Al/SBA-15 samples.

As inferred from Table 1 data, the *d*-spacing of the (1 0 0) plane is almost constant accompanying with the introduction of Cu, Cr, and Fe components. It is therefore believed that these metal species were finely distributed and mainly confined in the mesoporous channel as the extra-framework species in the forms of either cations or their oxides without obviously modifying the structural parameters of SBA-15. In contrast, an obvious shift of the main diffraction peak to the lower angle was observed along with aluminum addition, hinting that the incorporation of Al into the SBA-15 skeleton. The relatively longer Al–O bond length as compared to Si–O bond was thought to be the reason causing a downward shift of the small-angle diffraction peak as previously described by Zhang et al. [8].

Metals (Fe, Cu, Cr, and Al) and their constituents were invisible in the broad-angle XRD patterns for the metal-modified samples (not shown). However, the existence of these phases cannot be totally excluded as the formed particles are too tiny to be identified or the loading amounts are below the XRD detection limit.

The textural properties of the as-synthesized catalysts were studied by $N_2$ adsorption representing a typical IV isotherm and a clear H1-type hysteresis loop in Fig. 2, in accordance with the characteristic feature of mesoporous materials [6,8]. According to the report of Kaliaguine et al. [9], the initial increase in adsorption capacity at relatively lower pressures ($P/P_0 < 0.1$) is assigned to monolayer adsorption on the micropores' surface as well as monolayer and initial multilayer adsorption in the mesopores' intrawall. Thereafter, the upward deviation at higher $P/P_0$ of 0.4–0.8 is believed to be associated with the progressive filling of mesopores in the main channels by a process of capillary condensation. BET specific surface areas and pore structures of as-synthesized SBA-15-based catalysts are shown in Table 1 and Fig. 3. For the parent SBA-15, its BET surface area and total pore volume ($V_t$) were 645 $m^2$/g and 0.81 $cm^3$/g, respectively. It was noted that the surface area of SBA-15 support was reduced to some degree along with the active metals doping (especially for the Al-containing samples), following a decreasing order of SBA-15 > Fe/SBA-15 > Cu/SBA-15 > Cr–Al/SBA-15 ≈ Cr/SBA-15 > Fe–Al/SBA-15 > Cu–Al/SBA-15 > Al-SBA-15. The surface areas of Cu/SBA-15 and Fe/SBA-15 were comparable to that of bare SBA-15, indicating that the Cu and Fe components were well dispersed over the mesostructured silica without an obvious agglomeration. In the other cases, the loss of surface areas of (Cr, Cr–Al, Fe–Al, and Cu–Al)/SBA-15 is associated with the diminution of mesopore volumes likely caused by some pore blockage (Table 1). A similar phenomenon was once observed by Gallo during the Al insertion into the framework of SBA-16 leading to a significant decrease in specific surface area from 1000 to 463 $m^2$/g [10]. Pore diameters determined by the BJH method fall into the mesoporous range of 5–8 nm. It has been observed that a drop in the pore size and a rise in the wall thickness occur simultaneously with the addition of active components, indicating that some metal species were confined inside the SBA-15 channels.

In order to clarify the pore architecture of catalysts, TEM measurements have been carried out for the bifunctional Cu–Al/SBA-15 sample with the image of (1 0 0) and (1 1 0) planes, being respectively shown in Fig. 4a and b, exhibiting the orderly 2D hexagonal arrays with uniform pore sizes of about 6.3 nm and the parallel-arranged channels having wall thickness of about 4.9 nm, in good agreement with the corresponding values determined by $N_2$ adsorption (see Table 1). The long-range mesoporous-ordering characteristic reflects a good-quality of this SBA-15 structured material, without being remarkably disturbed due to the Al and Cu introduction. Moreover, inside the mesopore channel metal

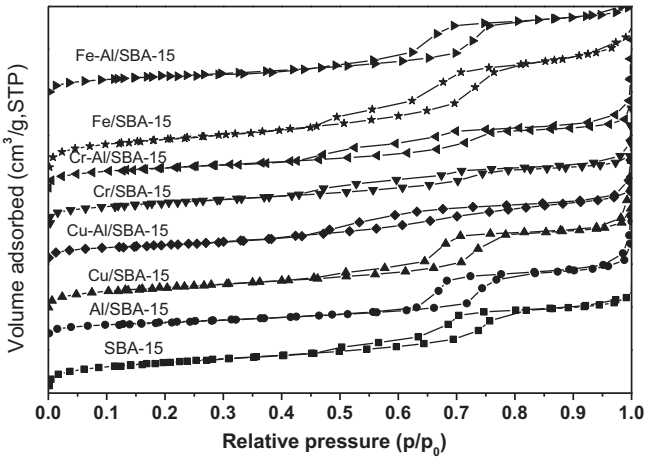


**Fig. 2.** $N_2$ adsorption/desorption isotherms of SBA-15, (Al, Cu, Cr, Fe)/SBA-15 and (Cu, Cr, Fe)-Al/SBA-15.

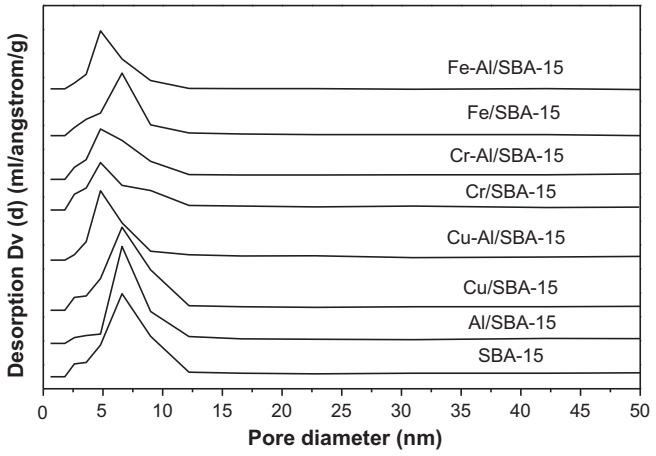


**Fig. 3.** Pore size distributions of SBA-15, (Al, Cu, Cr, Fe)/SBA-15 and (Cu, Cr, Fe)-Al/SBA-15.

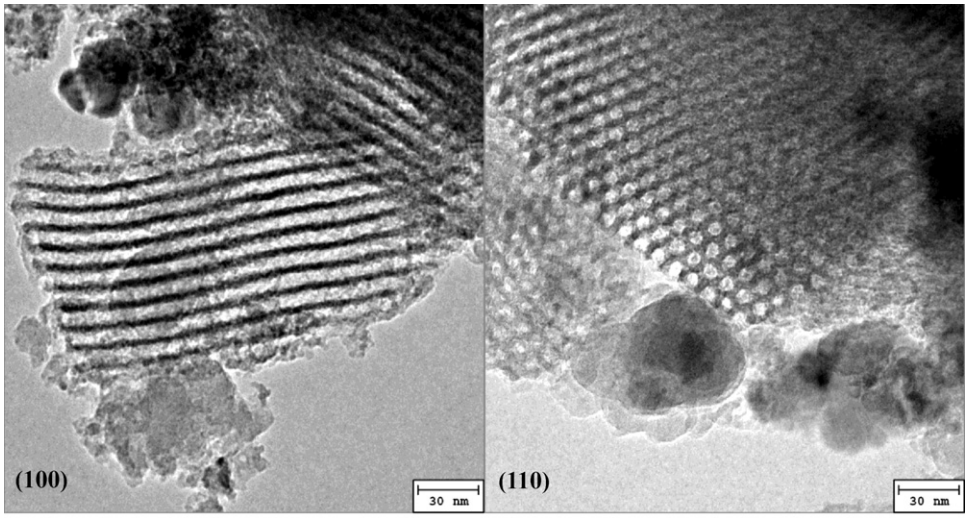


**Fig. 4.** TEM images of Cu–Al/SBA-15 sample from (a) (1 0 0) and (b) (1 1 0) reflections.

clusters were hardly observed, suggesting these metals were mainly distributed over the mesopore intra-surface and even incorporated into the framework of SBA-15. In addition, a minor impurity phase other than that of SBA-15 was found and is speculated to be amorphous alumina.

### 3.2. Redox properties

The reducibility of catalyst plays an important role in various reactions involving a redox mechanism. Fig. 5 represents the $H_2$-TPR profiles of SBA-15-based catalysts. The high stability of SBA-15 structure was confirmed due to the absence of a reduction peak in the investigated temperature region under a 5% $H_2$/Ar atmosphere. Since SBA-15 is nonreducible under the conditions for $H_2$-TPR, the slight $H_2$ consumption peak appearing at 621 °C in the TPR profile of Al/SBA-15 was accordingly ascribed to $Al^{3+}$ reduction. A multiple-step reduction was observed over Fe/SBA-15, showing a peak centered at 464 °C followed by a broad one at >794 °C. The former was attributed to the $Fe^{3+}$ to $Fe^{2+}$ reduction, the latter to the partial reduction of $Fe^{2+}$ to metallic iron according to our previous investigation [11]. Two peaks at 399 and 538 °C were discerned from the TPR profile of Fe–Al/SBA-15, corresponding to the reduction of $Fe^{3+}$ cations and iron oxides, respectively. The $FeO_x$ reduction occurring in a similar temperature region was previously reported [12,13]. In addition, the peak appearing on the TPR plot of Fe/SBA-15 for $Fe^{2+} \rightarrow Fe^0$ reduction totally vanished in the TPR plot of Fe–Al/SBA-15. As for the Cr/SBA-15 sample, the corresponding TPR profile showed an intense peak at 509 °C and a shoulder at its rising part (443 °C). These reducing peaks were believed to be related to the partial reduction of $Cr^{6+}$ ions and $Cr_2O_3$ as previously described [8]. It seems that Al incorporation is beneficial for $Cr_2O_3$ formation, displaying three overlapping peaks at 329, 437 and 543 °C. The latter one was again attributed to the $Cr^{6+} \rightarrow Cr^{3+}$ reduction, while the former two were likely caused by the reduction of $Cr_2O_3$ with different crystalline domains. It is believed that the bigger metal oxide is more readily reduced than the smaller one [14]. The sharp peak at 288 °C observed with the Cu/SBA-15 sample was ascribed to the reduction of $Cu^{2+}$ cations, as was done for Cu-ZSM-5 [15] and $LaFe_{0.8}Cu_{0.2}O_3$ [11]. It was noted that this copper reduction peak was shifted to lower temperature (247 °C) along with the Al incorporation, implying a better redox properties of Cu–Al/SBA-15.

### 3.3. Al status characterization

The type of Al coordination in both Al/SBA-15 and Cu–Al/SBA-15 was probed using $^{27}$Al MAS NMR with spectra being depicted in

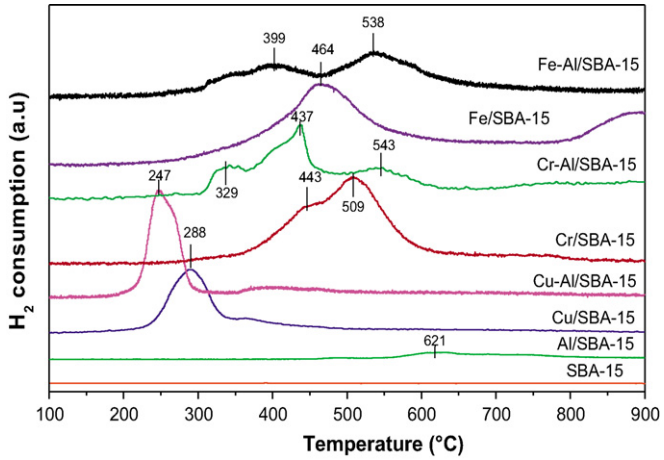


**Fig. 5.** $H_2$-TPR profiles of SBA-15, (Al, Cu, Cr, Fe)/SBA-15 and (Cu, Cr, Fe)-Al/SBA-15.

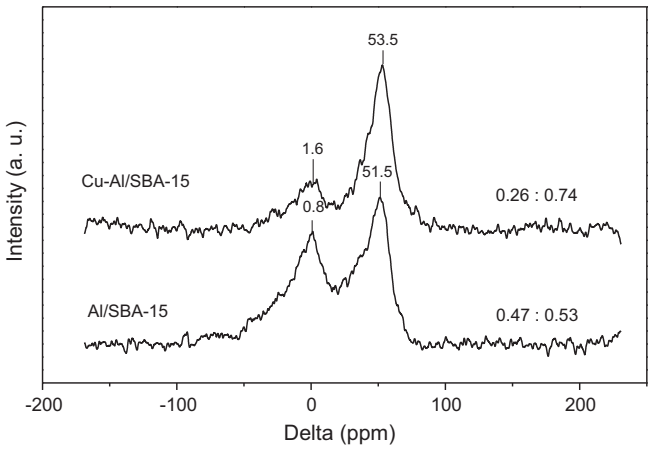


**Fig. 6.** $^{27}$Al MAS NMR of Al/SBA-15 and Cu–Al/SBA-15.

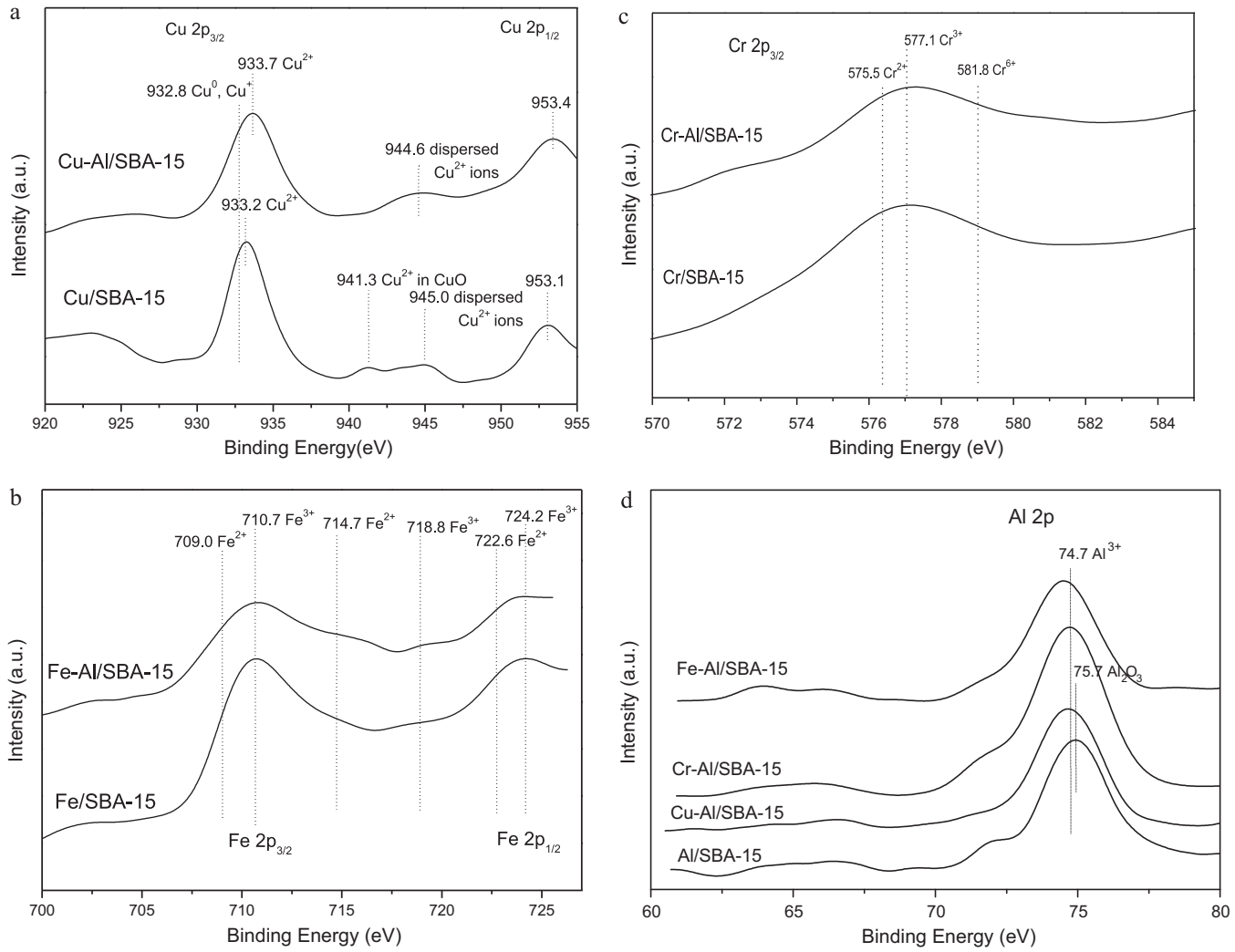


**Fig. 7.** XPS spectra of (a) Cu 2p for Cu/SBA-15 and Cu–Al/SBA-15; (b) Fe 2p for Fe/SBA-15 and Fe–Al/SBA-15; (c) Cr 2p for Cr/SBA-15 and Cr–Al/SBA-15; (d) Al 2p for Al/SBA-15 and (Fe, Cr, Cu)-Al/SBA-15.

Fig. 6. The Al/SBA-15 showed a NMR peak at ca. 54 ppm attributable to the tetrahedral framework aluminum ($Al^{IV}$) intra-wall formed along with another resonance peak at around 0 ppm belonging to the octahedral coordinated aluminum ($Al^{VI}$) outside the SBA-15 skeleton, according to the literature assignment [8,10,16]. The Al(tetrahedral)/Al(octahedral) ratio is 1.13 in the case of Al/SBA-15, suggesting that almost half of the aluminum in this sample existed in a tetrahedral state inside the SBA-15 wall while the other half likely remained mainly as alumina. These extra-framework aluminas might be the cause of a serious drop in the corresponding surface areas (see Table 1). Interestingly, the NMR peak at 0 ppm (associated with octahedral aluminum) for Cu–Al/SBA-15 was totally suppressed and the opposite occurred in the resonance peak at ~54 ppm (assigned to tetrahedral aluminum). This strongly suggested that Al nuclei have been mainly incorporated into the framework with the assistance of copper loading. As reported in the literature, similar interconversion between tetrahedral $Al^{IV}$ and octahedral $Al^{VI}$ was once realized by means of adjusting pH value or thermal treatment [15].

### 3.4. Analysis of surface metallic components

For the sake of getting insight into the surface composition and clarifying the nature of active sites, XPS was employed in this study as shown in Fig. 7a–d with the atomic concentrations of corresponding metals being reported in Table 2. As regards the $Cu_{2p}$, the main peaks observed in Fig. 7a were at BE ($2p_{1/2}$) = 953.1 eV and BE ($2p_{3/2}$) = 933.0 eV with its shake-up satellite. The valence of (divalent and/or reduced) copper species can be further differentiated according to their characteristic binding energies because only the $Cu^{2+}$ species ($3d^9$) shows a shake-up satellite peak located about 10 eV higher than the Cu $2p_{3/2}$ transition. As verified by Fig. 7a, $Cu^{2+}$ species were present over the surface of both Cu/SBA-15 and Cu–Al/SBA-15.

Due to the detection limit, minor amount of metal oxides ($MO_x$) in the prepared samples are commonly XRD undetectable. Nonetheless, the XPS is much more sensitive than XRD in detecting the $MO_x$ phase and the results obtained are helpful identifing the metallic status in M/SBA-15. For example, $Cu^{2+}$ species existing as highly dispersed ions can be distinguished from those in the bulk CuO according to the BE values of their satellite peaks. It is revealed based on the UV–vis measurement that the crystal field of isolated $Cu^{2+}$ ions (formed by ion-exchange with hydrogen atoms of hydroxyl groups of oxide support and most probably located on the surface with an octahedral or pseudo-octahedral environment) is weaker than that for $Cu^{2+}$ in bulk CuO particles (surrounded by four oxygen anions in a distorted square-planar symmetry). As a result, $Cu^{2+}$ in the CuO lattice usually shows a satellite peak lower than that for the well dispersed $Cu^{2+}$ ions. $Cu^{2+}$ species in both the bulk CuO and those dispersed as metallic ions were observed

**Table 2**
XPS elemental analysis of the mesoporous SBA-15-based catalysts.

| Sample | Surface atomic concentration (mol.%) | | | | | |
|---|---|---|---|---|---|---|
| | Si | O | Al | Cu | Cr | Fe |
| SBA-15 | 35.60 | 64.40 | – | – | – | – |
| Al/SBA-15 | 18.65 | 72.57 | 8.78 | – | – | – |
| Cu/SBA-15 | 35.47 | 64.14 | – | 0.39 | – | – |
| Cu–Al/SBA-15 | 35.86 | 59.86 | 3.87 | 0.41 | – | – |
| Cr/SBA-15 | 33.57 | 65.88 | – | – | 0.55 | – |
| Cr–Al/SBA-15 | 30.16 | 59.95 | 9.36 | – | 0.53 | – |
| Fe/SBA-15 | 38.08 | 60.73 | – | – | – | 1.1 |
| Fe–Al/SBA-15 | 27.46 | 64.74 | 7.36 | – | – | 0.44 |

for Cu/SBA-15 sample displaying BE satellite peaks at 941.3 and 945.0 eV in accordance with the literature report [17]. In contrast, only the highly isolated $Cu^{2+}$ ions were found for Cu–Al/SBA-15 sample.

As seen from Fig. 7b for Fe-containing SBA-15 catalysts, whose Fe $2p_{3/2}$ peaks are narrower and stronger than those of Fe $2p_{1/2}$ because of the spin-orbit (j–j) coupling; Fe $2p_{3/2}$ has degeneracy of four states while Fe $2p_{1/2}$ has only two. The comparison of Fe $2p_{3/2}$ binding energy with the reference data [18] allows us to assign the Fe $2p_{3/2}$ line at 710.7 eV and its satellite at 718.8 eV to the $Fe^{3+}$ ions. Thereafter, the shoulder line at 709.0 eV and its satellite at 714.7 eV were attributed to the partially reduced $Fe^{2+}$ ions. It is clearly seen from Fig. 7b that the surface iron species of the Fe-loaded samples mainly existed in the form of $Fe^{3+}$ species together with minor $Fe^{2+}$ ones.

In the light of the literature assignment [8,19,20], the Cr $2p_{3/2}$ signal approximately at BE = 577.1 eV was assigned to $Cr^{3+}$ and its shoulder at BE = 575.5 eV was ascribed to $Cr^{2+}$ (Fig. 7c). X-ray photoelectron bands appearing at BE = 579 eV confirmed the presence of $Cr^{6+}$ species [8]. It is clear that most of the chromium existed as trivalent cations, co-present with a small amount of $Cr^{6+}$ and $Cr^{2+}$ cations.

Three binding energies of Al 2p with values of 73.0, 74.5, and 75.4 eV were observed by Pashutski et al. [21] and thereafter assigned to pure metallic Al, $AlO_x$ in zeolite framework, and anhydrous $Al_2O_3$, respectively. XPS results in Fig. 7d suggest that most of the aluminum was successfully incorporated into the SBA-15 framework for all the Al-containing samples. The slight shift of the Al 2p peak to lower binding energy in the case of Cu–Al/SBA-15 with respect to Al/SBA-15 is likely due to the diminution of $Al_2O_3$ phase formation, in good agreement with the NMR result in Fig. 6. This additional phase of alumina was indeed visible via TEM (Fig. 4).

As seen from Table 2 for the elemental analysis of prepared SBA-15-based catalyst, the parent SBA-15 maintains a Si/O ratio close to that of $SiO_2$. A drop in the surface concentration of Si atom was found along with the Al introduction, suggesting that aluminum cover the surface of mesoporous silica prior to the metal components. The Si/O ratio of Cu/SBA-15 is similar to that of SBA-15, while its Cu content (0.39%) detected by XPS is much lower than the nominated value of 1% (see the experimental section). Therefore, we believe the highly dispersed copper was mainly loaded inside the intra-surface of mesoporous channel of SBA-15 or even incorporated into the skeleton of molecular sieve. The Cu contents in Cu/SBA-15 and Cu–Al/SBA-15 are almost constant regardless of whether the Al was introduced or not. A similar phenomenon occurs for Cr contents in the case of Cr/SBA-15 (0.55%) and Cr–Al/SBA-15 (0.53%). Co-existed Al led to an obvious decrease in the surface density of iron species. It was likely caused by the coverage of the iron species by Al-containing phase. The diminution of active metallic sites perhaps resulted in a decline in *de*$NO_x$ activity.

### 3.5. Activity test

The temperature dependence of NO and $C_3H_6$ conversions in the $C_3H_6 + NO + O_2$ reaction over the tested catalysts is shown in Figs. 8(a and b) and 9(a and b). NO conversion over the parent SBA-15 is marginal (below 5% at $T < 600\,^{\circ}C$). Nevertheless, the conversion was significantly improved by the introduction of active metallic components (Fig. 8a). Among monofunctional SBA-15 samples, a progressively increased NO conversion upon the rising temperature was found for Cr/SBA-15 catalyst. Moreover, highly dispersed

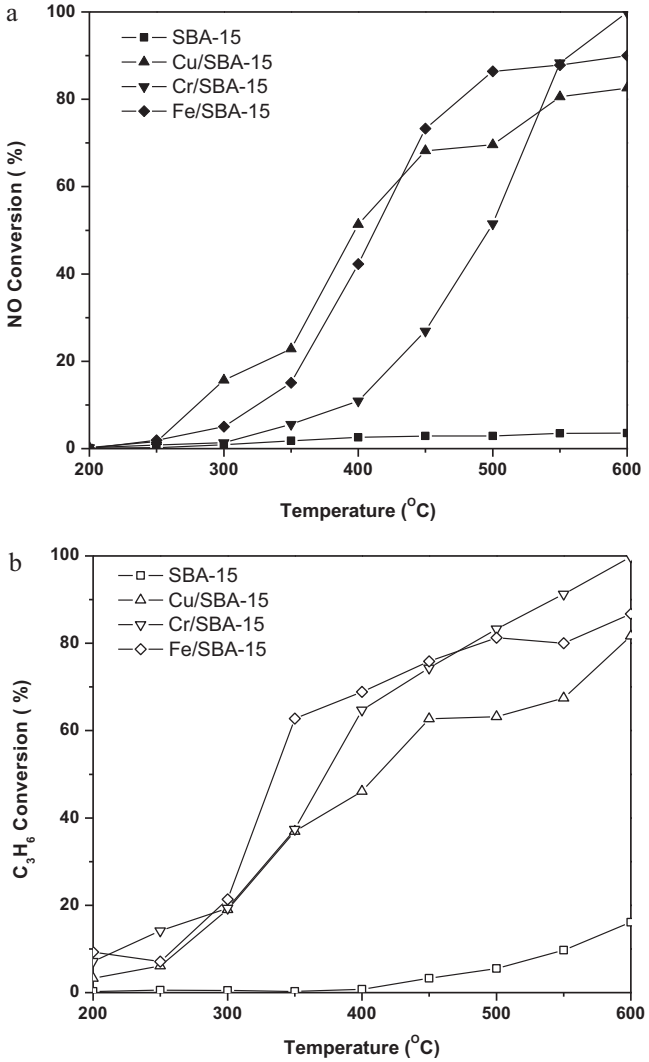


**Fig. 8.** (a) NO conversion and (b) $C_3H_6$ conversion in $C_3H_6 + NO + O_2$ reaction over SBA-15 and (Cu, Cr, Fe)/SBA-15, Conditions: 3000 ppm NO, 3000 ppm $C_3H_6$, 1% $O_2$, 60,000 $h^{-1}$.

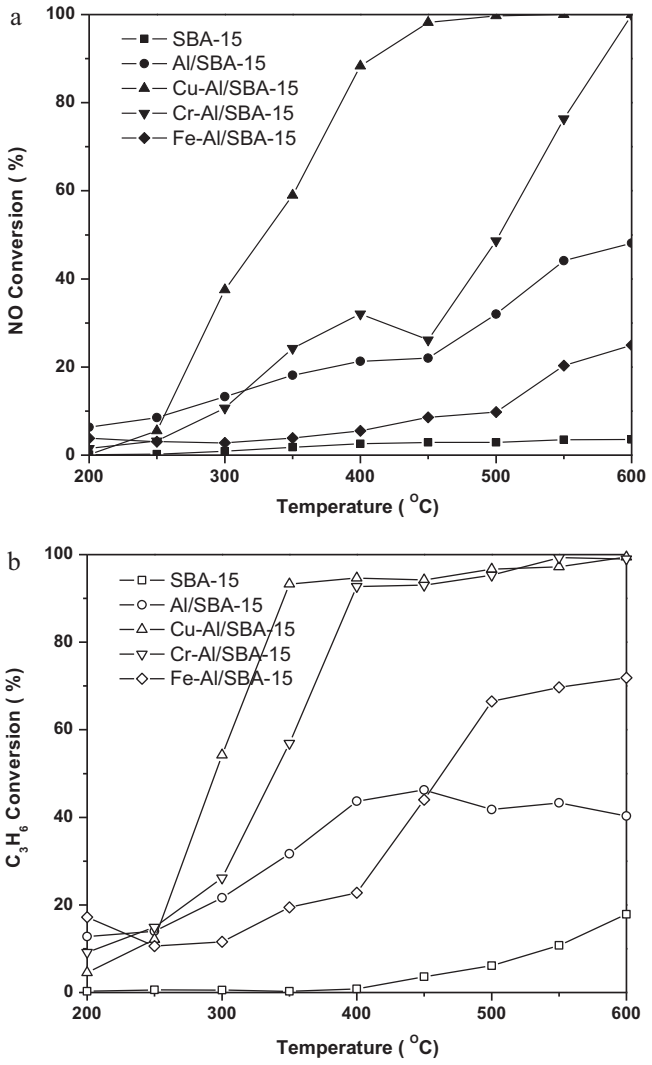


**Fig. 9.** (a) NO conversion and (b) $C_3H_6$ conversion in $C_3H_6 + NO + O_2$ reaction over Al-SBA-15 and (Cu, Cr, Fe)-Al/SBA-15, Conditions: 3000 ppm NO, 3000 ppm $C_3H_6$, 1% $O_2$, 60,000 $h^{-1}$.

copper and iron could lead to a further enhancement giving NO conversions of 83% and 90% at 600 °C, respectively. The promotion of $C_3H_6$ conversion of SBA-15 was also verified via metal dopings (Fig. 8b).

Al insertion in SBA-15 resulted in a moderated development of NO conversion (from 6% at 200 °C to 48% at 600 °C) with respect to the bare SBA-15 as shown in Fig. 9a. With a comparison between Figs. 8a and 9a, it was found that the Al doping played a distinct role on affecting three-way performances of co-loaded (Cu, Cr, and Fe) metallic components. A synergetic effect was achieved between copper and aluminum, resulting in an outstanding NO conversion over Cu–Al/SBA-15 starting at 200 °C and reaching almost 100% at a temperature as low as 450 °C together with 85% $C_3H_6$ conversion. Cr–Al/SBA-15, however, shows a NO conversion curve similar to that of Cr/SBA-15 except for a moderate promotion at temperatures <400 °C. Conversely, the Al loading led to an obvious inhibition in NO reduction for Fe/SBA-15, yielding values below 25% at the tested temperature range for Fe–Al/SBA-15 sample. $C_3H_6$ conversions in Fig. 9b roughly followed a decreasing order of Cu–Al/SBA-15 > Cr–Al/SBA-15 > Fe–Al/SBA-15 > Al/SBA-15. $N_2O$ and $NO_2$ yields were not addressed here due to their minor values. Moreover, $N_2$ selectivity was always above 90% at $T > 350$ °C for all tested samples (not shown).

### 3.6. Correlation between physicochemical properties and catalytic performance

Several mechanisms for NO catalytic reduction by $C_3H_6$ in the presence of $O_2$ have been documented in the literature with catalytic materials focusing on alumina support metals [22,23], perovskite-type oxides [11,24], and metal-promoted zeolites [25]. Based on early investigations for lean-burn NO reduction over silver/alumina catalysts finding that the promotion of SCR activity by Ag was realized by accelerating the NO oxidation, a bifuctional mechanism, in which the Ag component acting as the active centre favors the formation of nitrite or nitrate species while $Al_2O_3$ is beneficial for the reduction of $NO_2$ to $N_2$ by $C_3H_6$, has been proposed [22]. As a complementarity of the above mechanism, Iglesias et al. suggested a new reaction pathway for propene activation by Ag which involved the generation of acrylate species as a partially oxidized active intermediate [23]. Similarly, Wan et al. announced that adsorbed NO was oxidized into $NO_2$ upon Cu–Al-MCM-41 as the first step for SCR process simultaneously with a $C_3H_6$ pre-oxidation into acrolein or carboxylate species on the base of $NO_x$-TPD and FTIR studies [24]. Recently, a mechanism for the reaction of $NO + C_3H_6 + O_2$ occurring over La(Fe, Mn, Co)$_{1-x}$Cu$_x$O$_3$ perovskites was proposed by the authors, involving organo-nitrogen compounds (ONCs), likely generated from the interaction between nitrate species and adsorbed $C_3H_6$ with Cu ions in the B-site of perovskites regarded as the active sites available for the reactants adsorption and further interaction [11,24].

Based on the mechanism established in the literature [11,22–24], an attempt to correlate the catalytic performances of metal-promoted SBA-15 catalysts in NO catalytic reduction with the local structure of metal cluster and SBA-15 support has been made. Since the parent SBA-15 was proven to be inactive for catalytic reduction of NO with $C_3H_6$ in the presence of oxygen, the metallic components loaded were believed to act as the active sites, resulting in an obvious enhancement in NO conversion (Fig. 8a). The role of SBA-15 is accordingly supposed to be beneficial for the metals dispersion. In this study, the successful formation of SBA-15 mesoporous structure processing long-distance ordering and satisfactory surface areas (around 400–650 $m^2/g$) for the prepared materials, whose structural characteristics remained even after metal doping and further calcination at 500 °C, was presently verified by $N_2$ isothermal adsorption, XRD and TEM (Figs. 1–4). The characterization of local structure and coordination environment of active sites was further conducted by XRD (Fig. 1), TPR (Fig. 5), NMR (Fig. 6) and XPS (Fig. 7a–e). It was found that metals of Cu, Fe, and Cr were mainly distributed over the SBA-15 substrate as isolated metallic cations although a minor CuO phase in Cu/SBA-15 is evidenced by XPS pattern in Fig. 7a and iron oxides in Fe–Al/SBA-15 are verified by $H_2$-TPR in Fig. 5. In Fig. 8a, the diverse catalytic performances for NO reduction of the loaded metals are essentially ascribed to their chemical nature. Copper- and iron-containing catalysts are of special interest because there are active in the transition of nitrogen oxides [25,26], with the low-coordination isolated ions as active sites [27,28]. According to Fig. 7a and b, XPS analysis indicates that copper and iron components were fully distributed and mostly existing as $Cu^{2+}$ and $Fe^{3+}$ ions confined in the mesopore of SBA-15, whose mesoporous channel and superhigh surface favor metal dispersion and resistance to high-temperature sintering. An obvious improvement was achieved in the case of Cu/SBA-15 and Fe/SBA-15 samples, respectively yielding NO conversions of 83% and 90% at 600 °C, as compared to SBA-15 support (Fig. 8a). Furthermore, the satisfactory mobility of lattice oxygen of Cu/SBA-15, as evidenced by $H_2$-TPR in Fig. 5, is also responsible for its good *de*$NO_x$ activity.

Wan et al. announced that the Si/Al ratio had an effect on the electrostatic interaction between copper ions and the Al-MCM-41

framework as well as on the activity for NO reduction [29]. An effort to modify the local environment of SBA-15 by means of Al doping has been done here. Unlike the other elements (e.g. Cu, Fe, and Cr), the incorporation of some Al into the SBA-15 skeleton was confirmed based on NMR experiments (Fig. 6). The downward shift of low-angle diffraction peak of Al-loaded SBA-15 as compared to the unloaded SBA-15 also reflected the successful insertion of Al into the zeolite lattice (Fig. 1). The different role was played by Al on affecting the SCR performance of co-loaded metals of copper, chromium, and iron, as depicted in Figs.8a and 9b. The *de*$NO_x$ activity (especially at low temperature) of Cu/SBA-15 was obviously improved with the assistance of aluminum. Clearly, the presence of aluminum is beneficial for further developing the redox properties of Cu/SBA-15 catalyst showing a TPR peak at relatively lower temperature (247 °C) for Cu–Al/SBA-15 (Fig. 5). Moreover, copper species facilitate Al insertion into the framework of SBA-15 (Fig. 6). Furthermore, the formation of bulk CuO were detectable in the case of Cu/SBA-15 while this species was completely inhibited in the Cu–Al/SBA-15 samples with evidence from XPS (Fig. 7a). The isolated copper ions were verified to be more effective for adsorption and reduction of NO than CuO species, while the CuO species promoted the detrimental oxidation of propene leading to the lack of reducing agent [29]. The as-synthesized Cu–Al/SBA-15 sample with skeleton Al generally associating with the dispersed $Cu^{2+}$ ions thus displayed *de*$NO_x$ activity superior to that of Cu/SBA-15 with some CuO phases formed upon the extra-framework. In addition, Cu–Al/SBA-15 catalyst seems to involve into the "bifuctional mechanism" proposed by Bethke and Kung [22], in which $Cu^{2+}$ sites favorites the formation of nitrite or nitrate species while $AlO_x$ phase is beneficial for the further reduction of $NO_2$ by $C_3H_6$ towards $N_2$. Similarly, at <450 °C Cr–Al/SBA-15 exhibited a better SCR activity as compared to Cr/SBA-15, in accordance with the improvement of redox properties of Cr/SBA-15 via co-doping of Al; while the NO conversion at elevated temperatures essentially dependent on the concentration of isolated chromium species, thought as active centers for reactants adsorption, displaying a similar *de*$NO_x$ curve for Cr/SBA-15 and Cr–Al/SBA-15 at $T > 450$ °C. In contrast, the decline in NO conversion was found for Fe–Al/SBA-15 as compared to Fe/SBA-15, which could be explained by the possible coverage of active sites ($Fe^{3+}$) by the additional Al component based on the relatively weaker XPS peak of Fe $2p_{3/2}$ for Fe–Al/SBA-15 (Fig. 2b and Table 2). Otherwise, the appearance of iron oxides was also believed to be harmful for NO catalytic reduction. In short, the redox properties is crucially responsible for the low-temperature NO reduction by $C_3H_6$ likely via facilitating the corresponding reduction and/or oxidation process (e.g. pre-oxidation of $C_3H_6$, nitrite or nitrate formation) even at relatively lower temperatures. As the reaction temperatures became high enough, the reaction rate was somewhat correlated to the essential nature and the surface concentration of supported metals over SBA-15, which generally works as active sites for this SCR process. As a consequence, the synergistic effect was achieved between loaded copper and aluminum over high-surface-area SBA-15 support, resulting in a satisfactory *de*$NO_x$ activity of ~88% at 400 °C and almost complete at 450 °C in the case of Cu–Al/SBA-15 catalyst.

## 4. Conclusions

Mesostructured SBA-15 was obtained via hydrothermal synthesis with a highly structural ordering and a specific surface area of 645 $m^2/g$. As an ideal support, the as-synthesized SBA-15 was used for loading the active metallic components of Cu, Fe, and Cr. Due to good dispersion, metal-promoted mesoporous silica exhibits remarkable *de*$NO_x$ activity, which strongly depends on the essentially chemical nature of metals doped and their dispersities as evidenced by XRD, TPR, and XPS investigations. An optimal performance for NO catalytic reduction with $C_3H_6$ was herein achieved in the case of bifunctional Cu–Al/SBA-15. This synergistic effect between copper and alumina for NO catalytic reduction was accordingly ascribed to the promotion of redox properties of active copper species with the assistance of aluminum. Additionally, the Al presence is beneficial for suppressing the formation of CuO cluster, which is thought to be less active for NO-SCR, however, could facilitate the reductants consumption due to an unfavourable oxidation process as compared to isolated $Cu^{2+}$ ions. $T > 450$ °C, Cr/SBA-15 showed NO conversion curve similar to Cr–Al/SBA-15 sample, which was likely determined by highly dispersed Cr ions. The coverage of active $Fe^{3+}$ species due to the additional $AlO_x$ phase in the case of the bifuctional Fe–Al/SBA-15 resulted in a significant deactivation as compared to the monofuctional Fe/SBA-15. The *de*$NO_x$ performance of metal-supported SBA-15 catalysts was thereafter correlated to the chemical nature of supported metals, their redox properties and surface densities.

## Acknowledgements

The authors thank the National Natural Science Foundation of China under Grant (Nos. 20877007, 20821004, and 20977004), the Research Fund for the Doctoral Program of Higher Education of China (20090010120003), Chinese Universities Scientific Fund (ZZ1003), and the New Century Program for Outstanding Talents in University for the financial support.

## References

[1] M.D. Amiridis, T. Zhang, R.J. Farrauto, Appl. Catal. B 10 (1996) 203.
[2] A. Fritz, V. Pitchon, Appl. Catal. B 13 (1997) 1.
[3] T.E. Hoost, K.A. Laframboise, K. Otto, Appl. Catal. B 7 (1995) 79.
[4] Q. Shen, L. Li, Z. Hao, Z. Xu, Appl. Catal. B 84 (2008) 734.
[5] G. Delahay, B. Coq, L. Broussous, Appl. Catal. B 12 (1997) 49.
[6] D. Zhao, J. Feng, Q. Huo, N. Melosh, G.H. Fredrickson, B.F. Chmelka, G.D. Stucky, Science 279 (1998) 548.
[7] F. Hoffmann, M. Cornelius, J. Morell, M. Fröba, Angew. Chem. Int. Ed. 45 (2006) 3216.
[8] L. Zhang, Y. Zhao, H. Dai, H. He, C.T. Au, Catal. Today 131 (2008) 42.
[9] V. Hoang, Q. Huang, M. Eić, T. Do, S. Kaliaguine, Langmuir 21 (2005) 2051.
[10] J.M.R. Gallo, C. Bisio, L. Marchese, H.O. Pastore, Micro. Meso. Mater. 111 (2008) 632.
[11] R. Zhang, A. Villanueva, H. Alamdari, S. Kaliaguine, J. Catal. 237 (2006) 368.
[12] J.H. Park, J.H. Choung, I.S. Nam, S.W. Ham, Appl. Catal. B 78 (2008) 342.
[13] I. Melián-Cabrera, S. Espinosa, J.C. Groen, B. Linden, F. Kapteijn, J.A. Moulijn, J. Catal. 238 (2006) 250.
[14] R. Zhang, S. Kaliaguine, Appl. Catal. B 78 (2009) 275–287.
[15] B. Coq, D. Tachnon, F. Figueras, G. Mabilon, M. Prigent, Appl. Catal. B 6 (1995) 271.
[16] C. Wang, G. Zhu, X. Cai, T. Shang, L. Zhao, N. Li, R. Wang, Y. Wei, J. Li, S. Qiu, Top. Catal. 35 (2005) 25.
[17] J. Batista, A. Pintar, D. Mandrino, M. Jenko, V. Martin, Appl. Catal. A 206 (2001) 113.
[18] T. Yamashita, P. Hayes, Appl. Surf. Sci. 254 (2008) 2441.
[19] A.B. Gaspar, C.A.C. Perez, L.C. Dieguez, Appl. Surf. Sci. 252 (2005) 939.
[20] B. Liu, H. Nakatani, M. Terano, J. Mol. Catal. A 184 (2002) 387.
[21] A. Pashutski, A. Hoffman, M. Folman, Surf. Sci. 208 (1989) L91.
[22] K.A. Bethke, H.H. Kung, J. Catal. 172 (1997) 93.
[23] A. Iglesias-Juez, A.B. Hungría, A. Martínez-Arias, A. Fuerte, M. Fernández-García, J.A. Anderson, J.C. Conesa, J. Soria, J. Catal. 243 (2006) 171.
[24] R. Zhang, A. Villanueva, H. Alamdari, S. Kaliaguine, Appl. Catal. A 307 (2006) 85.
[25] Y. Wan, J. Ma, Z. Wang, W. Zhou, S. Kaliaguine, Appl. Catal. B 59 (2005) 235.
[26] G. Centi, S. Perathoner, Appl. Catal. A 132 (1995) 179.
[27] S.D. Peter, E. Garbowski, V. Perrichon, B. Pommier, M. Primet, Appl. Catal. A 205 (201) 147.
[28] M. Iwamoto, Catal. Today 29 (1996) 29.
[29] Y. Wan, J. Ma, Z. Wang, W. Zhou, S. Kaliaguine, J. Catal. 227 (2004) 242.